Oxygen Evolution Electrocatalysis in Acid: Atomic Tuning of Stability Number for Submonolayer IrO_x on Conductive Oxides from Molecular Precursors

Raina A. Krivina[‡,1] Matej Zlatar[‡,2,3] T. Nathan Stovall,[1] Grace A. Lindquist,[1] Daniel Eascalera-López,[2,4] Amanda K. Cook,[1] James E. Hutchison,[1] Serhiy Cherevko*,[2] and Shannon W. Boettcher*[1]

[1]*Department of Chemistry and Biochemistry*

University of Oregon, Eugene, Oregon 97403, USA

[2]*Helmholtz-Institute Erlangen-Nürnberg for Renewable Energy (IEK-11), Forschungszentrum Jülich, Erlangen, Germany*

[3]*Department of Chemical and Biological Engineering,*

Friedrich-Alexander-Universität Erlangen-Nürnberg, Egerlandstr. 3, 91058 Erlangen, Germany

[4]*Department of Interface Science, Fritz-Haber Institute of the Max-Planck Society, 14195 Berlin, Germany*

[‡]*Raina A. Krivina and Matej Zlatar contributed equally to this work.*

***Corresponding authors:** swb@uoregon.edu and s.cherevko@fz-juelich.de*

Keywords: *oxygen evolution reaction in acid, catalysis, submonolayer catalyst, iridium, titanium oxide*

Abstract. Proton-exchange-membrane water electrolyzers (PEMWEs) produce high purity H_2, withstand load fluctuations, and operate with a pure-water feed, but require platinum-group-metal catalysts for durability, such as IrO_2 and Pt, due to the acidic environment. At the anode, the slow oxygen evolution reaction (OER) requires high overpotential to achieve relevant current densities (> 2 $A \cdot cm^{-2}$) even with a high loading of IrO_2. Using a simple commercial 1,5-cyclooctadiene iridium chloride dimer precursor we synthesized sub-monolayer-thick IrO_x on the surfaces of conductive metal oxides, to make every Ir atom available for catalysis and reach the ultimate lower limit for Ir loading. We show that the reaction on $Sb:SnO_2$ and $F:SnO_2$ conductive oxides is surface-limited and that a continuous Ir-O-Ir network provides improved stability and activity. We cover IrO_x with a thin layer of acid-stable TiO_x by atomic-layer deposition. The effects of TiO_x on the catalyst's performance were assessed by ICP-MS coupled *in situ* with an electrochemical flow cell and *ex situ* by X-ray photoelectron spectroscopy. Tuning the binding environment of IrO_x by TiO_x addition enhances the intrinsic activity of the active sites simultaneously accelerating dissolution of the catalyst and the metal-oxide support. We illustrate the interplay between the support/catalyst/protective layer dissolution and OER activity and highlight the effects of annealing to densify the TiO_x passivation layer on stability/activity. These ultrathin supported Ir-based catalysts do not eliminate the long-standing issue of the catalyst and support instability during OER in acid, but do provide new insight into the catalyst/support interactions and may also be of utility for advanced spectroscopic investigations of the OER mechanism.

1. Introduction

Water electrolysis is a key source of renewable H_2.[1-2] Obtained using low or zero carbon-emissions energy, H_2 enables decarbonization of many economic sectors if costs are sufficiently low. Alkaline and proton-exchange-membrane water electrolysis (PEMWE) are the most-mature commercial technologies.[3] PEMWE offers benefits over alkaline electrolysis due to the use of a solid-polymer membrane and ionomer (perfluorosulfonic acids like Nafion) instead of a liquid electrolyte which enables operation at high current densities (>2 $A \cdot cm^{-2}$ at 1.7 V), load fluctuation, reduced product crossover, and the collection of compressed H_2.[3-5] The acidic nature of Nafion, however, limits the catalyst choice for PEM stacks to platinum-group metals (PGMs), mainly Ir and Pt, and restricts the materials for the stack components to acid-stable PGM-coated Ti.[3, 6-7] Alternatives to the PEMWE that use ionomer membranes with basic character are currently under development.[8-11]

While the Pt cathode operates at a low overpotential, the oxygen evolution reaction (OER) at the anode requires higher overpotentials even with the current benchmark catalyst, IrO_2.[12] Currently the price of the Ir catalyst is not the primary driving factor for electrolyzer costs, but it will play an increasingly dominant role once the reduction of other expenses is achieved and demand for precious metals increases.[13] Decreasing the Ir loading at the anode from 2-3 $mg \cdot cm^{-2}$ to < 0.4 $mg \cdot cm^{-2}$ is important for cost and scaling.[13-14] Many non-PGM materials have been studied as a replacement for IrO_2, but both activity and stability remain a serious issue for all acid non-PGM catalysts.[15-18]

One strategy to reduce PGM OER catalyst loading is via dispersing IrO_2 on an inexpensive support exposing more active sites for catalysis. To achieve long-term operation at high current density, the Ir-decorated support must be conductive and acid-stable. Unfortunately, there are only a few known nominally stable conductive support materials for harsh acidic conditions and even they dissolve after prolonged operation (for example, In, Sb, and F-doped SnO_2[19-22]; carbon[23]; Ta-doped SnO_2 aerogel[24]; TaC[25]). TiO_2 has also been studied as IrO_2 support.[26] Crystalline forms of TiO_2 are acid-stable but are semiconducting and electrically resistive. Thus, when a mixed IrO_2-TiO_2 catalyst is used, sufficient amount of Ir must be incorporated to create a conductive network (e.g. commercial catalyst from Umicore contains 75 wt. % of Ir).[27-29] Experimental and computational work suggest activity and stability improvements for IrO_2 in contact with TiO_2.[27, 30-31] The enhancement is attributed to tuning the surface charge density through metal-support

interactions.[30, 32] Thin layers of TiO_2 on Pt or IrO_2 also accelerate water dissociation for HER in acid and base.[33]

A possible approach to loading reduction thus might be through dispersing a thin layer of Ir on a conductive-oxide core support, and then protecting both with a thin layer of TiO_2 to achieve activity and stability enhancement. To test this architecture, we selected Sb- and F-doped SnO_2 (ATO and FTO, respectively) as conductive cores. In previous work, FTO showed higher stability than ATO, with no measurable dissolution from -0.34 to 2.7 V vs. RHE in acid.[19] ATO degrades due to Sb^{5+} solubility which leads to formation of an SnO_2-rich surface layer that impedes electron transport.[19] The presence of the catalyst and the protective layer, however, might affect the stability of the support materials.

Another consideration in loading reduction is the catalyst utilization in a membrane-electrode assembly (MEA).[3, 34] Some suggest that the active zone is limited to the region nearest to both the membrane and the metallic porous-transport layer[35] as defined by the ionic and electronic conductivities of the anode catalyst layer.[36] In this complex anode-reaction environment there thus remains a significant knowledge gap in how to prepare systems where every Ir atom is electrochemically active for catalysis while maximizing the activity and stability. The catalyst can also undergo dissolution/redeposition processes that ultimately lead to the loss of the active sites, especially in a three-electrode cell setup with excess liquid electrolyte. In an MEA, dissolution is likely slowed by the presence of a solid membrane impeding the transport of the Ir species away from the anode and perhaps leading to local redeposition.[37-40]

Every Ir atom might be made electrocatalytically active with a monolayer-thick IrO_x layer deposited on an electronically conductive support. An attempt to create a sub-monolayer-thick catalyst was made using a molecular catalyst $[Ir(pyalc)(H_2O)_2(\mu\text{-}O)]_2^{2+}$ that binds to metal-oxide surfaces. It remained stable for OER at pH 2.6 on *nano*-ITO electrode for several hours but eventually transforms into an amorphous IrO_x.[41] To improve performance, several metal-oxide supports were soaked in the $[Ir(pyalc)(H_2O)_2(\mu\text{-}O)]_2^{2+}$ solution multiple times and annealed to form an IrO_2.[21] Multiple soaks and post-deposition annealing improved stability compared to the initial molecular Ir complex, and the improvement varied for different metal oxides, but long-term durability was not achieved. In addition, $[Ir(pyalc)(H_2O)_2(\mu\text{-}O)]_2^{2+}$ is not commercially available which complicates further study and scaling.

Inspired by the reported influence of the nature of the metal oxide and the amount of bound Ir on activity,[21] here we report an approach to create, and fundamentally study, oxide-supported Ir using commercial 1,5-cyclooctadiene iridium chloride dimer precursor, $[(COD)IrCl]_2$. This supported Ir catalyst is not an example of a single-atom catalyst, but rather an approach to create and study an ultra-thin continuous network of IrO_x on a conductive support. We show that $[(COD)IrCl]_2$ adheres to the surface of metal oxides via a simple soaking procedure and upon annealing forms sub-monolayer-thick IrO_x catalysts. We study the OER properties of the sub-monolayer-thick IrO_x of different loadings in strong acid on ATO nanoparticles and planar FTO substrates, discovering that the increase of Ir loading not only improves activity but also enhances stability. By adding an ultrathin protective TiO_x layer by ALD, we further increase intrinsic activity but trigger the unexpected higher dissolution of Ir and underlying support, as demonstrated by changes to the stability number (the number of O_2 molecules evolved per atom of Ir lost)[42] measured via *in situ* electrochemical measurements coupled with inductively-coupled plasma mass spectrometry (ICP-MS). We show how this effect can be mitigated by annealing the catalyst after ALD. The changes to the catalyst chemical structure are tracked *ex situ* with X-ray photoelectron spectroscopy (XPS) that shows downshifts in Ir 4f binding energy upon TiO_x addition. We hypothesize that, in this new system, most Ir atoms are active during OER. Further, the surface characterization results are not obscured by the contribution from the bulk of the catalyst. This approach allows us to assess the impact of the binding environment on the intrinsic activity of Ir sites and develop strategies for engineering improved OER catalysts.

2. Experimental Section

2.1. Materials. Chloro(1,5-cyclooctadiene)iridium(I) dimer ($[(COD)IrCl]_2$, TCI) and antimony-doped tin-oxide (ATO) nanoparticles (~50 nm, Sigma Aldrich) were used as received. HPLC grade acetonitrile and toluene (Fisher Chemical) were used in synthesis. Isopropanol (IPA) and toluene used in washing the synthesized material and electrode ink preparation (Sigma Aldrich) were used as received. Fluorine-doped tin oxide (FTO) coated glass slides (resistivity ~ 13 Ω/sq) were obtained from Sigma Aldrich.

2.2. Synthesis of Ir-functionalized metal-oxides. ATO nanoparticles were vacuum dried at 80 °C overnight on a Schlenk line before bringing them into the glovebox under N_2. Acetonitrile and toluene used in synthesis were dispensed under N_2 from an LC Technology SP-1 solvent

system and transferred to the glovebox in an air-free flask. The 3.9 mM solutions of $[(COD)IrCl]_2$ in toluene and acetonitrile were prepared in the glovebox. Sixty milligrams of dried ATO nanoparticles were added to four vials: two with 3 mL of $[(COD)IrCl]_2$ in toluene; and two with 3 mL of $[(COD)IrCl]_2$ in acetonitrile. Each vial was capped with a Teflon-lined lid. The mixtures were left to stir overnight; one reaction for each solvent was kept at 100 °C, the other at room temperature. Then the particles were transferred to a centrifuge vial and washed with toluene or acetonitrile (depending on the solvent used in synthesis) twice to remove the remaining unreacted $[(COD)IrCl]_2$.

Planar 1 cm × 1 cm FTO substrates were sonicated in IPA, cleaned with O_2 plasma, and heated on a hot plate to 100 °C before being transferred to the glovebox. The substrates were placed into glass vials with Teflon-lined lids. A small amount of the 3.9 mM solution of $[(COD)IrCl]_2$ in toluene (just sufficient to cover the surfaces of the FTO substrates) was added into each vial with a small stir bar. The substrates were left to react overnight at 100 °C. Then the substrates were taken out of the glovebox and sonicated in toluene to remove any unreacted Ir dimer.

2.3. Characterization of Ir-functionalized nanoparticles and planar substrates. Elemental compositions of Ir-functionalized ATO nanoparticles and FTO substrates were determined with a Thermo Scientific ESCALAB 250 X-ray photoelectron spectrometer (XPS) using an Al Kα monochromated (20 eV pass energy, 500 μm spot size) source. The samples were charge-neutralized using an in-lens electron source. Spectra were analyzed using ThermoScientific Avantage 4.88 software. Peak binding energies were referenced to the C 1s hydrocarbon peak at 284.8 eV. Powder samples were prepared by drop-casting solutions of nanoparticles dispersed in IPA onto silicon wafers and allowing them to dry.

The amount of Ir on Ir-functionalized ATO nanoparticles (one soak; not annealed) was determined by inductively coupled plasma optical emission spectroscopy (ICP-OES, Teledyne Leeman Laboratories Prodigy High Dispersion). Approximately 10 mg of Ir-ATO were digested in 5 mL of concentrated HCl and diluted with 2% v/v HNO_3 for analysis. The recovered nanoparticles were analyzed by XPS to confirm Ir removal. The loading was confirmed by reacting 10 mL of 3.9 mM $[(COD)IrCl]_2$ with 200 mg of ATO and collecting aliquots of the solution before and after the reaction to determine extent of reaction. The diluted aliquots were analyzed with Perkin Elmer Lambda-1050 UV/Vis/NIR spectrophotometer. The loading for Ir-ATO after one and three soaks in Ir precursor solution (followed by a 350 °C anneal) was determined by using

energy-dispersive X-ray analysis (EDX) on a Titan 80-200 TEM (200 kV) after drop-casting dilute solutions of nanoparticles on a copper grid.

To track the dimer attachment to the surface of ATO nanoparticles in each solvent, optical absorption measurements were collected on Perkin Elmer Lambda-1050 UV/Vis/NIR spectrophotometer. Aliquots (0.25 mL) of the $[(COD)IrCl]_2$ solutions were taken before adding ATO nanoparticles and at different time intervals during synthesis, diluted to 2.5 mL, and analyzed from 250 to 800 nm with a scan resolution of 1 nm.

NMR spectra were collected on Bruker Avance III-HD 600 MHz NMR spectrometer. The 3.9 mM $[(COD)IrCl]_2$ solutions were prepared with toluene-d_8 and acetonitrile-d_3 (Cambridge Isotope Labs) and were analyzed before and after reacting with ATO nanoparticles for 5 h without further dilutions.

Triphenyl silanol (TPS) and tris(*tert*-butoxy) silanol (TBS) were dissolved separately in toluene-d_8 in the glovebox under inert atmosphere. ^{1}H NMR spectra of the initial solutions were recorded. To the 1-mL solutions of TBS and TPS, 2 mL of 3.9 mM $[(COD)IrCl]_2$ solution in toluene-d_8 was added. The mixed solutions were set on a hot plate at 100 ℃ with stirring for 1 h. ^{1}H NMR spectra of the solutions after 1 h of mixing were recorded.

The electron microscopy and chemical composition images of Ir-functionalized nanoparticles were collected on a Titan 80-200 TEM equipped with an EDX detector (200 kV). The samples for analysis were prepared by drop-casting dilute solutions of ATO and Ir-functionalized ATO nanoparticles in IPA on Cu grids and allowing them to dry.

2.4. Iridium layer growth on metal-oxide powder and planar substrates. $[(COD)IrCl]_2$ (~60 mg, 0.09 mmol) was dissolved in 20 mL of anhydrous toluene in the glovebox. The solution was filtered through a syringe filter and 400 mg of ATO were added. The nanopowder was allowed to react in the Ir-containing solution overnight at 100 ℃. The reacted powder was washed in toluene twice via centrifugation and annealed in the box furnace at 350 ℃ for 3 h. The annealed powder was ground, then dried in the oven overnight at 100 ℃ before being transferred to the glovebox. The powder was reacted with $[(COD)IrCl]_2$ solution in toluene for a second time. At the end of the second overnight reaction the powder was again washed, annealed, and returned to the glovebox to react with $[(COD)IrCl]_2$ a third time. After the third soak the nanopowder was again washed in toluene and annealed at 350 ℃ before electrochemical testing. The catalyst shell growth

on a planar FTO substrate was accomplished the same way. The powder samples and the planar substrates were analyzed with XPS after each reactant soak.

2.5. Thermogravimetric analysis of [(COD)IrCl]$_2$. A 10 mg sample of [(COD)IrCl]$_2$ was placed in an Al pan and loaded into a thermogravimetric analyzer (TA Instruments TGA Q500). The sample was heated from room temperature to 600 ℃ at 5 ℃/min in air (Figure S1).

2.6. Atomic-layer deposition (ALD) of TiO_x on Ir-functionalized ATO nanopowder and FTO substrates. ATO nanopowder after one and three soaks in Ir dimer precursor solution in toluene annealed at 350 ℃ for 3 h was placed in the ALD vacuum chamber on a piece of Al foil with raised edges. A fine metal mesh was placed over the foil to prevent powder loss during the deposition process. The powder was decorated with TiO_x via 5 ALD cycles. The deposition was carried out at 250 ℃ using tetrakis(dimethylamido)titanium (TDMAT) and water as TiO_x precursors. The precursors were alternating with a 0.05 s pulse of water and a 0.5 s pulse for TDMAT allowing a 60 s purge between each precursor.

Ir-functionalized FTO substrates (1 cm × 1 cm) after one and three soaks in the Ir dimer solution in toluene and annealing at 350 ℃ for 3 h were placed in the ALD vacuum chamber and reacted with the same precursors as the nanopowder but at 150 ℃ with a 1-s water pulse, 0.25-s TDMAT pulse, and a 15-s purge between the precursors. After deposition some of the substrates were additionally annealed at 400 ℃ for 1 h.

The thickness of the resulting TiO_x protective layers was measured on a Si witness wafer with a Woollam M44 spectroscopic ellipsometer. Measurements were collected at the incident angles of 45°, 50°, 55°, 60°, 65°, 70°, 75° in the range 240 - 1688 nm. The analysis is based on least-squares regression analysis. The deviation is represented by the mean square error (MSE).

2.7. Electrode preparation and electrochemical measurements in a three-electrode cell. The annealed Ir-functionalized nanopowder was mixed with IPA to prepare a 60 mg/mL catalyst ink. IPA and O_2 plasma cleaned FTO substrates (~1 cm × 1 cm) were spin-coated with the ink at 3000 rpm (Laurell WS-400-6NPP-LITE) and annealed at 350 ℃ for 1 h. Ir-functionalized planar FTO substrates were used after the 3-h 350 ℃ annealing. The substrates were fabricated into electrodes by making an ohmic contact to the FTO surface with a Sn/Cu coil wire and Ag paint. The coil was then fixed in a five-inch glass tube. The contact and the tube were insulated by epoxy (Loctite 9460) and cured in the oven. A BioLogic SP300 potentiostat was used in three-electrode mode for electrochemical measurements. The electrodes were tested in 0.1 M $HClO_4$

with a Pt wire as the counter electrode and a saturated calomel electrode (SCE; 0.24 V vs SHE in sat. KCl) as a reference electrode. To determine the catalyst activity towards OER, three CVs (0.5 V – 1.5 V vs SCE) were collected. Then the electrodes were held at 0 $mA \cdot cm^{-2}$ for 180 s, followed by 5 $mA \cdot cm^{-2}$ for 300 s, and again at 0 $mA \cdot cm^{-2}$ for 180 s. Electrochemical data were corrected for uncompensated series resistance R_u, which was determined by equating R_u to the minimum total impedance in the frequency regime in the high frequency range (0.1 to 1 MHz) where the capacitive and inductive impedances are negligible, and the phase angle was near zero. After testing the electrodes were rinsed, dried, and analyzed by XPS.

2.8. Preparation of working electrodes for electrochemical scanning flow cell (SFC) measurements. Ir-FTO working electrodes were used as prepared in sections 2.4 and 2.6, while Ir-ATO working electrodes were prepared by drop-casting catalyst spots from previously prepared inks. To achieve a predefined ink concentration of 0.66 mg/mL, the corresponding amount of powder sample was weighed and dissolved in ultrapure H_2O (Merck Milli-Q, 18 MΩ, total organic carbon <3 ppb) and isopropanol in a 7:1 ratio. After dissolving the samples, perfluorinated Nafion ionomer solution (Sigma Aldrich, 5 wt %) was added as a binder in a 4:1 catalyst-to-ionomer weight ratio. Inks were then sonicated for 10 min with 4-s on and 2-s off pulses using a probe sonicator (Branson Ultrasonics SFX150) to achieve homogenous dispersion. The pH of the prepared inks was adjusted to ~11 with 1 M aq. KOH, followed by drop-casting of 0.2 µL aliquots on Au foil plates (25 × 25 mm, 99.95 %, Alfa Aesar) mirror polished with alumina suspensions (sequentially from 1 to 0.5 and finally 0.03 µm particle diameter). Each catalyst spot had a diameter of approximately 1.3 mm, measured on the Keyence VK-X250 profilometer.

2.9. SFC-ICP-MS electrochemical experiments. To estimate the corrosion stability of Ir on planar FTO substrates and ATO nanoparticles, an inductively coupled plasma mass spectrometer (ICP-MS, Perkin Elmer, NexION 300x and 350x) was connected to the SFC. The setup enabled the downstream detection of dissolved species during electrochemical measurements. Electrical and physical contact between the SFC opening and the samples is achieved by an XYZ-translation stage (Physik Instrumente), applying a vertical compression force of ~850 mN (measured by a force sensor, ME-Meßsysteme). In one case, the working electrode consisted of Ir-functionalized ATO powder, drop-casted on Au foil, while in the other case, of as-prepared Ir-FTO substrates. On the inlet tube of the SFC, a graphite rod (Sigma Aldrich, 99.995% trace metal basis) encased in a glass compartment was connected as a counter electrode, while on

the outlet side of the cell, the capillary channel was connected to a reference Ag/AgCl electrode (Metrohm, 3 M KCl). This channel ends close to the surface of the working electrode, thus minimizing R_u. All electrodes were connected to a Gamry Reference 600 potentiostat, and the setup was controlled by LabVIEW software. The Ar-purged 0.1 M $HClO_4$ used as an electrolyte was prepared by diluting $HClO_4$ (Suprapur 70%, Merck) with ultrapure water. Electrode potentials are referenced to the reversible hydrogen electrode (RHE) scale, calibrated daily against H^+/H_2 on polycrystalline Pt foil. The catalyst dissolution rate was measured at an electrolyte flow rate of ~3.2 $\mu L \cdot s^{-1}$, determined by the ICP-MS peristaltic pump. To ensure optimal working conditions, ICP-MS was optimized daily using NexION Setup Solution (PerkinElmer) and calibrated for all investigated metals by three-point calibration. Calibration solutions of 0.5, 1, and 5 ppb concentrations (Certipur ICP-MS Standard, Merck) were prepared daily. The drift and performance of the system throughout the measurements were monitored by several internal standard solutions (Re, Rh, Te, Sc, conc. 10 $\mu g \cdot L^{-1}$), chosen based on similar first ionization potential and mass (Certipur ICP-MS Standard, Merck).

To assess activity-stability properties, the electrodes were held at 0 $mA \cdot cm^{-2}$ for 180 s, followed by 0.5 $mA \cdot cm^{-2}$ for 300 s, and again at 0 $mA \cdot cm^{-2}$ for 180 s. Obtained analyte signal was recalculated to concentration using the calibration curve and normalized by the flow rate and geometric area of the working electrode (see previous publications for details[43-45]). All measurements were replicated three times.

3. Results and Discussion

3.1. Synthesis and characterization of Ir-functionalized metal oxides

3.1.1. Metal-oxide surface functionalization. The synthesis was developed using simple commercial precursors. $[(COD)IrCl]_2$ is similar in cost to IrO_2 on a per-Ir basis, and, due to the presence of COD and Cl ligands, dissolves well in polar and non-polar solvents. The solution of $[(COD)IrCl]_2$ is, however, unstable in air and upon contact with water, so the synthesis was carried out in the glovebox under N_2.

FTO films on glass and ATO nanoparticles, both conductive and relatively stable in acid, were selected to test whether $[(COD)IrCl]_2$ would adhere to metal-oxide surfaces.[19, 46-47] FTO nano-powder and ATO-coated glass are not widely commercially available and therefore were not studied. To determine the optimal conditions for the reaction, polar and nonpolar solvents,

acetonitrile and toluene, respectively, were tested. The stability of $[(COD)IrCl]_2$ in toluene and acetonitrile (ACN) at room temperature and at 100 °C was confirmed by analyzing the UV-vis spectra of the dimer solutions after 25 h in the glovebox. No changes to the spectra were observed. Then ATO nanoparticles (surface area of 47 $m^2 \cdot g^{-1}$) were added to the Ir precursor solutions and stirred for 25 h with aliquots taken every few hours for UV-vis analysis. One reaction for each solvent was kept at room temperature, one at 100 °C.

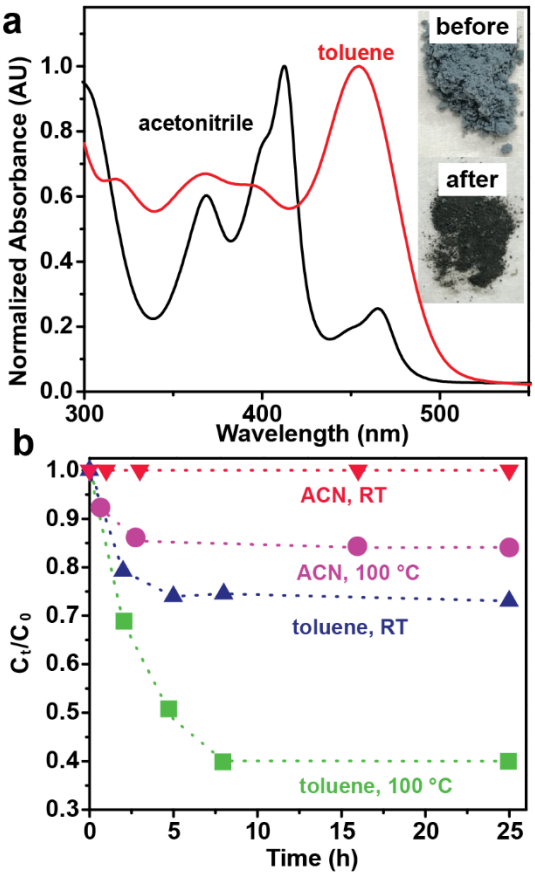

Figure 1. UV-vis analysis shows more $[(COD)IrCl]_2$ surface absorption in toluene. A) Normalized UV-vis spectra of $[(COD)IrCl]_2$ taken in acetonitrile (black) and toluene (red). Inset: ATO before and after reacting with $[(COD)IrCl]_2$ in toluene. b) The change in concentration of the $[(COD)IrCl]_2$ stock solutions in acetonitrile and toluene during the reaction with ATO nanoparticles at room temperature and at 100 °C.

Figure 1a shows the UV-visible spectra of freshly made $[(COD)IrCl]_2$ solutions in toluene and ACN. The spectra in the two solvents look different with the λ_{max} in toluene at 454 nm and in ACN at 413 nm. The difference might be due to interactions of coordinating ACN ligands with the metal centers compared to weak interactions with toluene.

The absorbance at λ_{max} was used to calculate the change in concentration over time (C_t/C_0; **Figure 1b**). The spectra of $[(COD)IrCl]_2$ in toluene and ACN do not change shape as the reaction progresses, just decrease in intensity, suggesting that the dimer preserves its initial structure in the solutions (Figure S2). No change in $[(COD)IrCl]_2$ concentration was observed for the reaction carried out in ACN at room temperature. When the solution was heated to 100 °C, ~15% of $[(COD)IrCl]_2$ attached to the nanoparticles. In room-temperature toluene, ~25% of $[(COD)IrCl]_2$ attached to ATO; at 100 °C, 60% attached. The nanoparticles reacted with $[(COD)IrCl]_2$ in the ACN and the toluene solutions changed color from light blue to dark green (inset of **Figure 1a** and Figure S3 for ATO color change in toluene). The attachment of $[(COD)IrCl]_2$ to ATO nanoparticles happens during the first 5-7 h of the reaction. Afterwards the concentration of $[(COD)IrCl]_2$ in the solutions remains unchanged. The lack of continuous dimer loss from the solution up until the end of the reaction suggests that the adhesion reaction is surface-limited.

The difference in the amount of the dimer adhered to ATO in ACN and toluene is likely due to the difference in the interactions between $[(COD)IrCl]_2$ and the solvent molecules. Polar ACN might arrange itself at the surface of the metal-oxide nanoparticles preventing the dimer from interacting with the surface. ACN might also interact with the Ir, modifying the affinity for the metal-oxide surface. Toluene, being nonpolar and non-coordinating, should not introduce substantial activation barriers for $[(COD)IrCl]_2$ to access the surface of ATO. The surface adsorption/reaction rate increases with temperature indicating a kinetically controlled process. The difference in the amount of $[(COD)IrCl]_2$ adhered to ATO in toluene and ACN also suggests a different mechanism of attachment.

The reactions of ATO nanoparticles and $[(COD)IrCl]_2$ at 100 °C were repeated in deuterated toluene (toluene-d_8) and ACN (ACN-d_3) and monitored with ^{1}H NMR. No substantial changes to the Ir dimer structure were observed during the reactions consistent with $[(COD)IrCl]_2$ adhesion to ATO without the loss of ligands (Figure S4). Given that more $[(COD)IrCl]_2$ attaches to ATO in toluene at 100 °C, we chose these reaction conditions for further study.

3.1.2. Iridium functionalization of ATO and FTO supports. Using the established reaction conditions, we soaked ATO nanoparticles and FTO planar substrate in the 3.9 mM solution of $[(COD)IrCl]_2$ in toluene overnight at 100 °C, then analyzed them with XPS (Table S1), TEM-EDX, and ICP-OES.

XPS analysis of the unreacted $[(COD)IrCl]_2$ powder confirms the 1:1 Ir:Cl ratio. The Ir 4f peak was fitted with two doublets (Ir $4f_{7/2}$ at 61.2 and 62.8 eV) (**Figure 2a**). The binding energies of the $4f_{7/2}$ peaks matched literature values for $[(COD)IrCl]_2$.[48] The peak at 61.2 eV was attributed to Ir^{1+} while the peak at higher binding energy was assigned to the hydroxylated Ir surface species.[48] In our case, the high-binding-energy peak likely arises from the topmost layer of the powder degrading in air as the sample is loaded into the XPS chamber. The Ir 4f peak of $[(COD)IrCl]_2$ attached to ATO nano-powder was fit with one set of Ir 4f peaks ($4f_{7/2}$ centered at 62.0 eV) (**Figure 2a**). The Ir:Cl ratio remained 1:1 suggesting that the dimer attaches or absorbs to the metal oxide intact and is also consistent with monolayer limited growth and all Ir species in the same chemical environment. The shift to higher binding energy of the anchored dimer compared to the free-standing powder might originate from dimer/metal-oxide interactions. The Ir 4f peak of the dimer adhered to a FTO substrate was also fit with one set of peaks at 62.1 eV (**Figure 2a**). The Ir:Cl ratio was also 1:1.

Determining the Ir loading on the acid-stable supports proved a challenge. Ir-ATO compounds are known to be digestion-resistant including conditions such as aqua regia and HF.[49] Once Ir-functionalized ATO and FTO were annealed (350 °C), no digestion conditions appeared capable of removing Ir completely (e. g. conc. HF; boiling piranha; boiling conc. HCl; high potentials, E > 2 V). Another issue with planar FTO substrate specifically was small surface area to bind enough Ir to be detectable by ICP-OES after digestion/dilution. Thus, we focused on Ir-ATO particles. We were able to remove Ir from Ir-functionalized ATO before annealing by conc. HCl digestion. The Ir loading on ATO nanoparticles was 58 ± 7 ng_{Ir}/cm^2_{ATO} (or ~ 2.7 wt. % Ir). This loading agrees with the wt. % of Ir on Ir-ATO by EDX (3.7 ± 1.4 wt. % Ir). To further confirm the loading, aliquots of 3.9 mM $[(COD)IrCl]_2$ solution were collected before and after reacting with a measured amount of ATO. The decrease in absorbance (~ 26%) corresponds to ~ 3.5 wt. % Ir on the ATO. The distribution of Ir on ATO was mapped with TEM-EDX (**Figure 2b**).

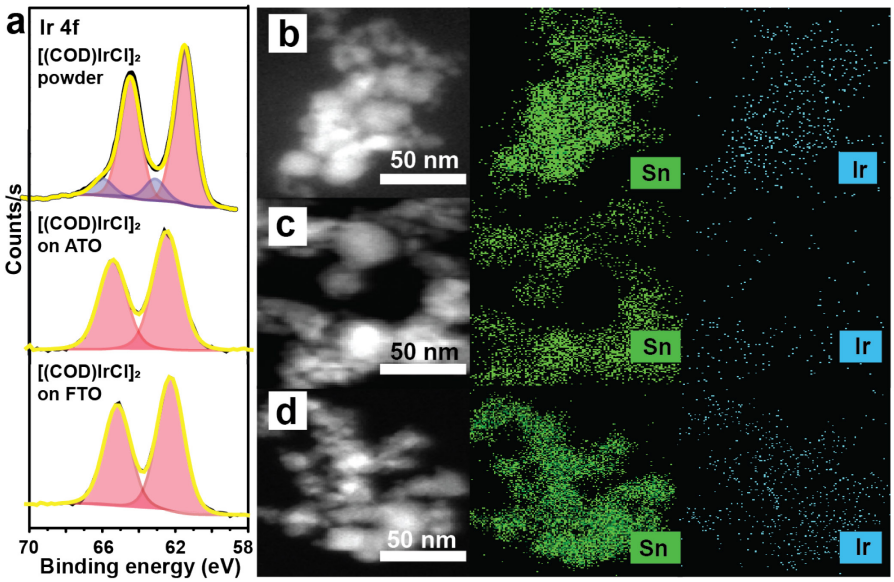

Figure 2. **Surface characterization confirms Ir on ATO.** a) XPS of Ir 4f in $[(COD)IrCl]_2$ powder and after the dimer attached to ATO nanoparticles and FTO substrate. TEM-EDX images of Ir-functionalized ATO nanoparticles (b) after one soak in the precursor solution; (c) after 350 °C annealing; and (d) after 600 °C annealing.

To access the mechanism of $[(COD)IrCl]_2$ attachment to metal-oxide surfaces, an experiment was conducted with soluble metal hydroxyls: triphenyl silanol (TPS) and tris(*tert*-butoxy) silanol (TBS). The Ir dimer was mixed with the metal hydroxyls in tolune-d_8, allowed to react for 1 h, and the mixtures were analyzed with ^{1}H NMR (Figure S5). No evidence of $[(COD)IrCl]_2$ binding to the terminal -OH of TPS or TBS was observed suggesting the dimer likely adheres to ATO and FTO through physical absorption instead of covalent bonding.

3.1.3. Iridium-oxide film growth on the surface of conductive supports. Applications such as PEMWE might require increasing Ir loading to achieve higher intrinsic activities and industry-relevant current densities. Since the dimer can adhere to the surface of a metal-oxide support through a simple soak, more dimers should attach to the Ir species already on the surface if the ligands are removed, thus forming a Ir-O network. By TGA (Figure S1), most of the mass loss occurs between 200 and 310 °C (~43%). COD ligands comprise ~53% of $[(COD)IrCl]_2$ by mass, Cl ~8 %. Chloride ligands are known to require higher temperatures for removal.[50] A 5% mass loss was observed between 310 °C and 600 °C.

We annealed Ir-ATO powder at 350 ℃ and 600 ℃ to study the loss of ligands. At 350 ℃, half of Cl is lost and the surface Ir:Sn ratio stays unchanged (~7 %). Ir 4f peak changes from one to two doublets (Ir $4f_{7/2}$ at 62.4 and 63.5 eV) (**Figure 3b**), likely due to the dimer breaking and bonding to the surface while some Ir remains bound to Cl. After 600 ℃, all Cl is lost, the surface Ir:Sn ratio decreases by 50%, and only one state of Ir present (Ir $4f_{7/2}$ centered at 62.4 eV) (Figure S6). The change in the surface Ir:Sn ratio likely comes from agglomeration and/or mixing of the Ir with the ATO, so the XPS signal of Ir decreases. Sn is known to diffuse during high-temperature annealing from SnO_2 into neighboring oxides, such as hematite.[51] TEM-EDX maps of atom distribution (**Figure 2b, c, d**) do not show any clear changes after annealing. The 350 ℃ anneal was chosen for Ir-shell growth to avoid mixing/agglomeration.

ATO nanoparticles and the FTO substrate were soaked three times in $[(COD)IrCl]_2$ solution in toluene overnight at 100 ℃ with a three-hour 350 ℃ anneal between soaks. The surface Ir:Sn ratio increases with every soak (**Figure 3a** and S7a) illustrating controlled Ir-O coating thicknesses. After three soaks in $[(COD)IrCl]_2$ solution ATO nanoparticles (3S-ATO) had a surface Ir:Sn ratio of 25% (**Table 1** and **Figure 3a**). As discussed above, once annealed, Ir cannot be removed from ATO or FTO by digestion. The EDX of 3S-ATO showed 8.3 ± 2.8 wt. % Ir which corresponds to ~ 170 ng_{Ir}/cm^2_{ATO}. The Ir 4f peak was fit with two doublets ($4f_{7/2}$ peaks at 62.2 and 63.5 eV), similarly to 1S-ATO (**Figure 3b**). New Ir states appearing upon annealing are likely due to partial crystallization of the Ir-O network towards Ir^{3+} or a mixture of Ir^{3+} and Ir^{4+}.[52-53]

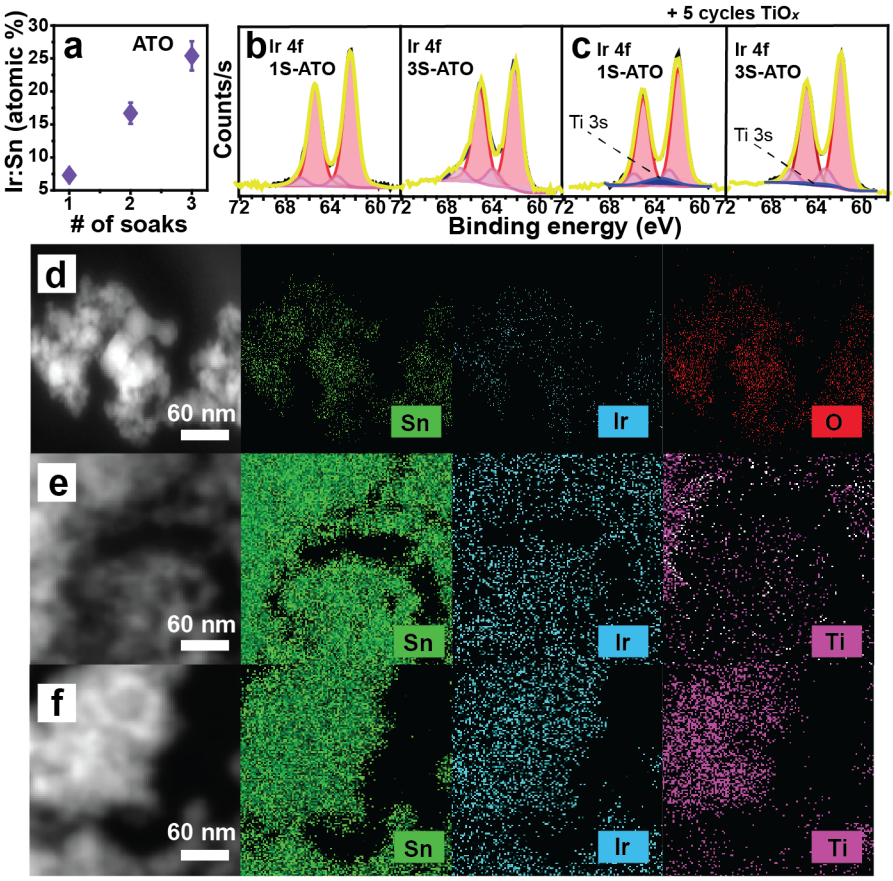

Figure 3. **Ir shell growth and TiO_x deposition on metal-oxide substrates.** a) The Ir:Sn ratio increases with every consecutive soak of ATO nanoparticles in the Ir precursor solution. b) XPS spectra of Ir 4f peaks collected on ATO substrates that were soaked in the Ir precursor solution once or three times and annealed at 350°C. c) XPS spectra of Ir 4f peaks collected on the ATO substrates soaked in the Ir precursor solution once or three times followed by TiO_x deposition by ALD. Elemental mapping by TEM-EDX of Sn, Ir, and Ti on (d) 3S-ATO; (e) 1S-ATO-5-TiO_x and (f) 3S-ATO-5-TiO_x.

The FTO substrate soaked/reacted once with the $[(COD)IrCl]_2$ solution (1S-FTO) gains a second Ir $4f_{7/2}$ doublet at 63.5 eV after the 350 °C annealing as does the Ir-functionalized ATO powder (Figure S7b); the surface Ir:Sn ratio is 6% and after three reaction cycles increases to 38% (Figure S7a). The 3S-FTO sample has three Ir 4f doublets with $4f_{7/2}$ at 62.4, 63.6, and 64.8 eV (Table S1). The doublet at the high binding energy might originate from Ir-F or new Ir-Cl bonds forming as the result of annealing.

3.1.4. TiO_x protection layers. ALD enables the growth of conformal metal-oxide films of desired thickness at low temperatures on planar as well as porous or powder substrates.[54-55] The

addition of TiO_x via 10 cycles of ALD to planar IrO_2 was reported to increase the OER specific activity in 1.0 M H_2SO_4 nine-fold.[30] The improvement was attributed to tuning the surface electronic properties and optimizing the point of zero charge.[30] Aside from enhancing the intrinsic activity of IrO_x, an overlayer of TiO_x might support better catalyst stability toward deleterious dissolution side reactions given its inertness in acidic conditions. The Ir-functionalized ATO nanoparticles and FTO substrates were decorated with five cycles of TiO_x via ALD at 150 °C (for FTO) and 250 °C (for ATO) using a tetrakis(dimethylamido)titanium (TDMAT) precursor (see Table S2 for thicknesses). Higher deposition temperature was used on the nanoparticles to facilitate binding to less-exposed surfaces, along with longer purge time to allow more time to remove the unreacted precursor trapped in the powder. With only a few cycles of TiO_x deposited, however, we do not expect a conformal coverage which is a limitation of this study. The microscopy performed on similar architectures did not provide sufficient evidence to determine accurately the completeness of the coverage.

The XPS analysis of 1S-FTO and 3S-FTO shows Ir 4f shifting to lower binding energy upon TiO_x addition (~0.2 eV for 1S-FTO; ~0.7 eV for 3S-FTO) (Figure S8a, c). No shifts in Ir 4f binding energy were observed for 1S-ATO and 3S-ATO (Figure S9). The shift in binding energy might indicate electron donation from Ti to Ir or to the underlying support. The absence of the energy shift in the nano-powder samples might results from less TiO_x bound to the surface or absence of charge density changes at the surface of ATO. These samples were tested for OER activity and durability as discussed below.

Table 1. Surface elemental composition of Ir-functionalized substrates before and after electrochemical testing (EC) determined by XPS.

Sample	Ir:Sn (atom. %)		Ti:Sn (atom. %)	
	before EC	after EC	before EC	after EC
1S-FTO	5.7 ± 0.3	3.9 ± 1.1		
3S-FTO	38.5 ± 5.7	56.3 ± 0.7		
1S-FTO-5-TiO_x	15.2 ± 2.0	5.5 ± 0.5	14.7 ± 0.4	9.1± 1.4
3S-FTO-5-TiO_x	110.9 ± 9.3	76.6± 2.4	77.8 ± 3.8	10.4 ± 1.1
3S-FTO-2-TiO_x	103 ± 30	50 ± 27	22.8 ± 2.3	undetected
3S-FTO-20-TiO_x	42.3 ± 2.1	114 ± 14	182 ± 11	143 ± 12
3S-FTO-2-TiO_x (400 °C)	74.7 ± 4.7	47 ± 19	14.5 ± 2.7	3.3 ± 0.7
3S-FTO-5-TiO_x (400 °C)	44.9 ± 4.6	80 ± 12	36.9 ± 1.3	36.1 ± 2.9
3S-FTO-20-TiO_x (400 °C)	46.9 ± 2.0	79.8 ± 6.3	114.3 ± 7.9	156.9 ± 8.3
1S-ATO	7.2 ± 0.1	6.4 ± 0.1		
3S-ATO	12.3 ± 0.7	12.9 ± 1.0		
1S-ATO-5-TiO_x	6.7 ± 0.2	6.8 ± 0.3	3.0 ± 0.1	2.7 ± 0.3
3S-ATO-5-TiO_x	20.6 ± 0.1	5.1 ± 0.5	15.3 ± 1.7	2.2 ± 0.2

3.2. Electrochemical performance of Ir-functionalized metal-oxide supports.

Although electrochemical measurements provide insight into catalyst activity, any conclusions regarding electrocatalyst stability are incomplete and sometimes misleading without understanding the dissolution of the catalyst and the underlying support. We used a scanning electrochemical flow cell (SFC) coupled with downstream ICP-MS to track the potential-dependent dissolution and activity therefore complementing the traditional three-electrode cell measurements. Catalyst stability was estimated by the stability number (S-number), a dimensionless metric that is independent of the number of active sites, surface area, or loading. It represents the number of O_2 evolved per Ir atom dissolved in the electrolyte, detected by ICP-MS. The S-number is calculated by dividing the total integrated charge over time (assuming near 100% faradaic efficiency, such that practically all the current goes to OER) with the amount of catalyst dissolved. High S-number values indicate a stable catalyst.[42]

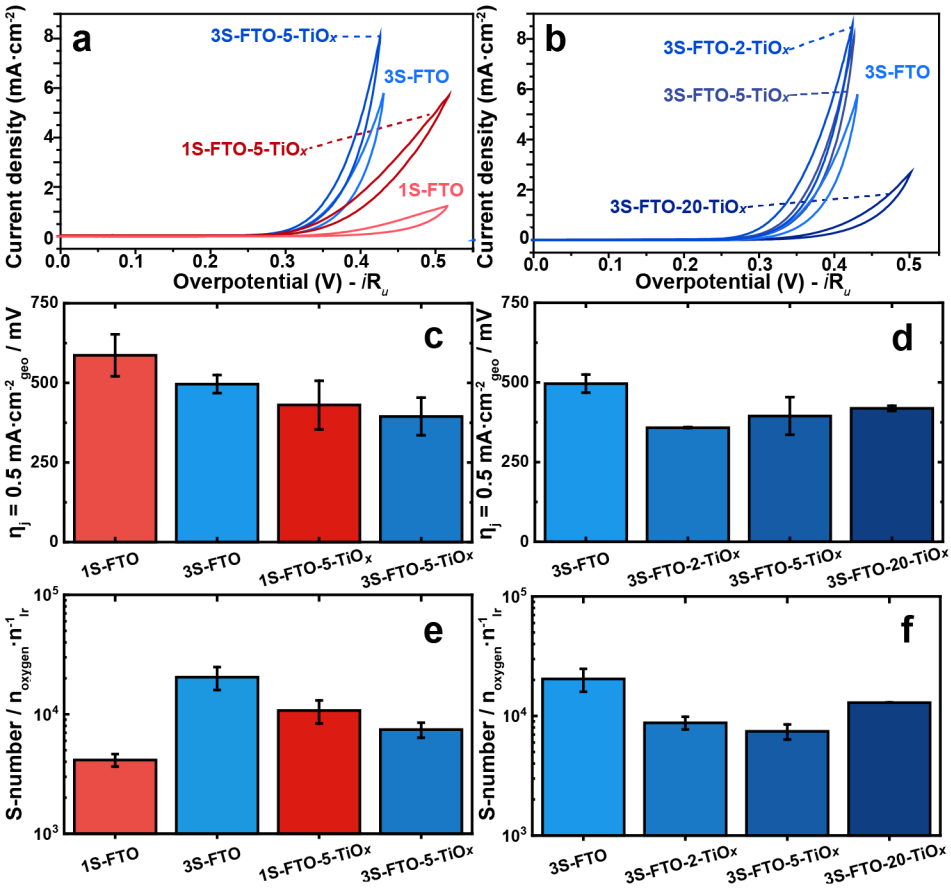

Figure 4. A thin layer of TiO_x on Ir-FTO enhances activity. a, b) Cyclic voltammetry data for Ir-functionalized FTO substrates collected in 0.1 M $HClO_4$ at pH ~1. c, d) Compilation of OER overpotentials (η) for the different Ir-based catalysts measured at geometric current densities of 0.5 mA cm^{-2}. Overpotential values were taken at the end of the chronopotentiometry measurements where samples reached quasi-steady-state operation. e, f) S-numbers of different Ir-based catalysts prepared in this work. S-numbers values are calculated from a galvanostatic hold at 0.5 mA·cm^{-2}. For representative dissolution profiles see Figures S10, S11 and S13.

3.2.1. Influence of Ir loading on Ir-FTO activity-stability relationships. Increasing the catalyst loading on the support, in principle, will affect the performance of the catalyst through providing more active sites available for catalysis and by creating a network of Ir-O-Ir on the surface (in place of possible isolated sites) that may have different catalytic properties. Cyclic voltammetry and the measured OER activity at 0.5 mA·cm^2 show that higher loading (3S-FTO vs 1S-FTO) leads to an earlier OER onset and a lower overpotential (**Figure 4 a, c**). Ledendecker *et al.* reported a similar increase in OER activity as a result of varying the amount of attached IrO_x on FTO substrates through the soaks in Ir precursor.[21] Here we discover that the increase in OER activity is accompanied by a substantial increase in stability (**Figure 4e**). The stability number of

3S-FTO is ~5× higher than the 1S-FTO sample (2×10^4 compared to 4×10^3). However, while S-numbers of both samples, especially 3S-FTO, is comparable to metallic Ir/hydrous IrO_x films (S ~ $10^4 - 10^5$), it is still significantly lower to that of crystalline IrO_2 films (S ~ $10^6 - 10^7$).[42, 56] The stability improvement might originate from the higher Ir loading of 3S-FTO and thus lower mass-normalized currents applied during the galvanostatic hold, or that the anchoring strength of IrO_x onto FTO is weaker than on other IrO_x.[57] The activity improvement of 3S-FTO compared to 1S-FTO is likely related to the need for significant Ir-O-Ir type connectivity in the catalyst as opposed to more-isolated IrO_x sites that may be present in 1S-FTO.

XPS analysis of the Ir 4f peak in the pristine 1S-FTO and 3S-FTO samples suggests a higher Ir coverage on 3S-FTO as evidenced by an increase in the Ir:Sn ratio from 5.7% to 38.5% (Figure S7a). There is also a gradual increase in the as-synthesized Ir oxidation state as more catalyst layers are added that may lead to a more-dissolution-resistant structure (Table S1). A 5 $mA \cdot cm^{-2}$ hold was then applied to the substrates in a bulk three-electrode-cell. The post-operation XPS analysis of 1S-FTO shows no shifts in the binding energy for the main Ir 4f peak but the second doublet at higher binding energy disappears (Figure S8b) which is likely due to the more-complete loss of Cl (as seen in XPS data) and Ir oxidation. The Ir:Sn ratio also decreases from 5.7 to 3.9% supporting the dissolution observed by ICP-MS (**Table 1**). Post-operation 3S-FTO Ir 4f peak was fit with three doublets similarly to the pristine sample (Figure S8b), but shifted to a slightly lower binding energy perhaps due to the loss of the remaining Cl ligands and the formation of a more stable network on the surface of FTO. The Ir:Sn ratio, surprisingly, increases after the current hold from 38.5 to 56.3 % despite the observed Ir dissolution, indicating higher surface Sn dissolution than Ir. The dissolution profiles (Figure S10) for 1S-FTO show sharp increases of dissolved Ir during the initial 0 $mA \cdot cm^{-2}$ hold and at 0.5 $mA \cdot cm^2$. While no current is passing, the amount of Sn dissolved for this sample is in the range of Sn loss in 3S-FTO during the 0.5 $mA \cdot cm^{-2}$ hold (~0.72 $ng \cdot cm^{-2}$ and ~0.80 $ng \cdot cm^{-2}$, respectively). The 3S-FTO primarily loses Ir while the current is passing. Thus, the same amount of Sn is lost during OER (at 0.5 $mA \cdot cm^{-2}$) in both 1S and 3S samples, but Ir dissolution occurs at a faster rate for 1S-FTO. The difference in rates of Ir dissolution might explain the decrease in Ir:Sn ratio in 1S-FTO and its increase in post-operation 3S-FTO observed by XPS.

3.2.2. TiO_x-coated Ir-FTO thin films and activity-stability relationships. Addition of 5 cycles of TiO_x by ALD resulted in improved OER activities regardless of the Ir loading (**Figure 4a and c**). For both 1S-FTO and 3S-FTO samples, the OER overpotential drops by ~150 and ~100 mV, respectively (**Figure 4c).** In the case of 1S-FTO, adding a TiO_x capping layer significantly increased its stability (S-number $\approx 1.0 \times 10^4$), while its activity increased to values comparable to the pristine 3S-FTO. Contrary to the 1S-FTO sample, Ir stability worsens for 3S-FTO (S-number decreases to 7.4×10^3) (**Figure 4e**). Even though both samples show a similar amount of Ti dissolved, for sample 3S-FTO-5-TiO_x, Ti dissolution is accompanied by almost two times higher Sn dissolution compared to 1S-FTO, 1S-FTO-5-TiO_x, and 3S-FTO (Figure S13a). If the surface coverage of IrO_x on FTO was not complete after just one soak in $[(COD)IrCl]_2$, TiO_x could bind to FTO in addition to Ir which may suppress Sn dissolution, and in turn reduce Ir dissolution during OER. By binding to both IrO_x and FTO, TiO_x might be able to form a more-effective protective layer. After three soaks in $[(COD)IrCl]_2$ the FTO surface should have a higher IrO_x coverage allowing less TiO_x to bind directly to the FTO support.

The binding energy of the Ir 4f peak in the 3S-FTO sample shifts down by ~0.7 eV upon TiO_x deposition and for 1S-FTO-5-TiO_x it shifts by ~0.2 eV. The Ir 4f binding energy shift upon TiO_x addition is not consistent with previous reports. Finke *et al*. describes a downshift in binding energy of Ti 2p upon TiO_2 addition to a layer of IrO_2 with no energy shifts observed for Ir 4f.[30] Kasian *et al.* observed a downshift in Ti 2p binding energy when Ir content was increased for Ir-Ti alloys.[31] The shift in the binding energy of Ti 2p is attributed to the charge transfer from Ir surface to TiO_2. In our system, the ultrathin layer of IrO_x is interacting with an n-type metal oxide (FTO) that can apparently transfer charge density to the catalyst layer resulting in a downshift of the Ir 4f peak. For the sample with higher Ir loading (3S-FTO), not all layers of Ir are affected by the charge transfer from FTO due to screening. Indeed, Ir 4f in 3S-FTO is at a higher binding energy than in 1S-FTO (Table S1). Addition of TiO_x seems to enhance the transfer of charge density to the Ir layer. The observed electronic effect between TiO_x, IrO_x, and the support can be similarly thought of as an interfacial redox reaction due to differences in free energy of the species. We hypothesis that there the electronic effect is a partial charge transfer driven by differences in (electro)chemical potential of the electrons and the need to equilibrate.

XPS analysis of the 1S-FTO and 3S-FTO samples with 5 cycles of TiO_x before and after electrochemical testing is shown in Figure S8. The Ir and Ti dissolution observed by ICP-MS is confirmed by the decrease of Ir:Sn and Ti:Sn ratios in the samples after electrochemical testing (**Table 1**).

3.2.3. Influence of TiO_x ALD number of cycles on Ir-FTO thin films: Activity-stability relationships. We prepared 3S-FTO with 2, 5, and 20 cycles of TiO_x by ALD. 1S-FTO was not studied in this experiment due to the high overpotentials required to drive OER at 0.5 mA cm^{-2} on that sample. The thickness of the TiO_x layers was measured on a witness Si wafer by ellipsometry (Table S2). The cyclic voltammetry test shows OER activity improvement with 2 and 5 cycles of TiO_x and a decrease in activity with 20 cycles (**Figure 4b**). Based on the SFC test, the addition of 2, 5 and 20 cycles of TiO_x decreased OER overpotentials by 138, 102 and 78 mV, respectively (**Figure 4d**). The sample with 20 cycles of TiO_x exhibited the least improvement likely due to thicker TiO_x blocking active sites and increasing mass-transport resistances. We note that the trends in activity are slightly different for CV (**Figure 4b**) and CP (**Figure 4d**) measurments. This observation highlights that for such samples, apparent activity depends on the testing protocol.[58] The CV and SFC-ICP-MS data demonstrate that only a small amount of TiO_x is necessary to enhance catalytic activity.

The trend in decreased stability (loss of Ir) observed for 3S-FTO-5-TiO_x also holds for the samples with 2 and 20 TiO_x cycles (**Figure 4f**). According to the dissolution profiles, the 3S-FTO protected by 2 cycles of TiO_x loses as much Sn as 3S-FTO-5-TiO_x (~2.17 ng·cm^{-2}), but Sn dissolution goes down for 3S-FTO-20-TiO_x (0.64 ng·cm^{-2}) (Figure S13b). With 20 cycles, TiO_x might form a more conformal layer and reduce Sn loss. Ir loss is the least for 3S-FTO-20-TiO_x compared to the samples with 2 and 5 TiO_x cycles.

Higher numbers of TiO_x ALD cycles also affects the stability of the formed TiO_x layer. While all TiO_x was lost from 3S-FTO-2-TiO_x during the current hold (according to XPS, **Table 1**), the sample with 20 cycles of TiO_x only lost as much Ti as 3S-FTO-5-TiO_x (Figure S13b). The ratio of Ir:Sn decreases for the samples with 2 and 5 cycles of TiO_x, but not for 3S-FTO-20-TiO_x. The partial loss of TiO_x apparently exposed more Ir for XPS analysis thus decreasing the surface Ti:Sn ratio while increasing the Ir:Sn ratio. Interestingly, Ti 2p remains at the same binding energy with increase in TiO_x cycles (Figure S14). The shift in Ir binding energy and the absence of the

shift in Ti indicates that the addition of TiO_x tunes the IrO_x/FTO interactions rather than influences IrO_x directly.

Thus, only 2 cycles of TiO_x (~0.14 nm) cause the activity improvement compared to unprotected 3S-FTO but also surprisingly trigger higher Ir, Ti, and Sn loss observed for 3S-FTO-2-TiO_x and 3S-FTO-5-TiO_x. The tradeoff between having the active sites accessible while protected must be balanced to achieve stable long-term performance.[59-60] Markovic *et al*., for example, argues that a stable oxide is inactive during OER and connects the catalyst's transition to higher oxidation states with dissolution and surface-defect formation resulting in a higher activity.[59] Such a transition can happen either with or without participation of lattice oxygen in the OER, with the former apparently causing higher dissolution.[57, 61-62]

3.2.4. Influence of post-ALD annealing on TiO_x-Ir-FTO thin films: Activity-stability relationships. To improve stability, we annealed the samples at 400 °C after the addition of the TiO_x capping layer. The activity of most of the annealed samples is in the same range compared to unprotected 3S-FTO, except for ones with 5 cycles of TiO_x that improve. However, all annealed samples have lower activity than before annealing (**Figure 5b**). The CVs show a slight decrease in activity for the samples with 2 and 5 cycles of TiO_2 and a more-considerable activity loss for the sample with 20 cycles. (**Figure 5a**).

After the additional anneal, the samples exhibit higher stabilities. The samples with 2, 5, and 20 cycles of TiO_x show 2.5-, 1.2-, and 1.6-times higher S-numbers than the samples that were not annealed after ALD (**Figure 5c**). The stability improvement might originate from changes in Ir and Ti crystallinity and oxidation states after heating at 400 °C. The Ir 4f for the post-ALD annealed samples shifts to higher BE consistent with higher oxidation state: 0.8 eV for 3S-FTO-2-TiO_x; 0.3 eV for 3S-FTO-5-TiO_x; and 0.1 eV for 3S-FTO-20-TiO_x (Figure S15a). Cl is almost completely gone from the surface following the additional annealing. Geiger *et al.* reported that significant IrO_2 is formed by increasing the annealing temperature from 300°C to 400 °C producing a more-stable but less-OER-active rutile structure.[52] No trend in binding energy shift was observed for Ti 2p – it goes up or down in energy by 0.1-0.3 eV, roughly the error in the measurement. Lin *et al.* reported an increase in surface roughness by heating TiO_2 films at 400 °C, followed by slight densification and the formation of anatase phase.[63]

Given how thin the layers of TiO_x and IrO_x are, they likely intermix during annealing forming new bonding environments rather than agglomerate to form nanoparticles. This hypothesis is supported by the changes in the elemental ratios calculated for the samples (**Table 1**). There is a decrease in Ti:Sn ratios for all post-ALD annealed samples suggesting that TiO_x is no longer solely on top. The Ir:Sn ratios also decrease for the samples with 2 and 5 cycles of TiO_x. The Ir:Sn ratio does not change after annealing for 3S-FTO-20-TiO_x, suggesting Sn cannot diffuse through the thicker TiO_x layer. Interestingly, the Ti:Ir ratio for 3S-FTO-2-TiO_x and 3S-FTO-5-TiO_x does not change after annealing at 400 °C, while for 3S-FTO-20-TiO_x the Ti:Ir ratio goes down after annealing. This data shows there may already be mixing of Ir and Ti in the first few layers of ALD TiO_x as synthesized, while annealing at 400 °C allows interdiffusion through the thicker 20-cycle TiO_x capping layer.

The stability, measured by the amount of dissolution during the OER, improves for Ti and Sn on post-ALD samples as well as for Ir. There is a 3-4 times lower Ti dissolution (Figure S13c). The Sn dissolution goes down to the level observed for 3S-FTO with the highest number of TiO_x cycles.

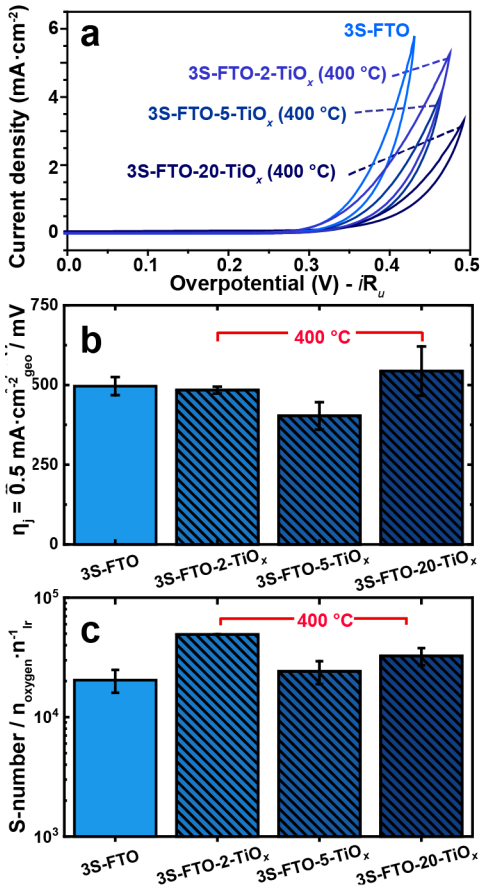

Figure 5. Post-ALD annealing improves stability but lowers activity. a) CVs collected in 0.1 M $HClO_4$ on the TiO_x-protected samples annealed at 400 °C after ALD. b) Overpotential at 0.5 $mA \cdot cm^{-2}$ and c) S-number for the post-ALD annealed samples. The OER activity is comparable to 3S-FTO but is lower than before annealing for all samples. There is a significant improvement in stability after additional annealing (prior to ALD, the samples had already been annealed at 350 °C for 3 h, as discussed in the experimental section)

After electrochemical testing, the Ir 4f peak in 3S-FTO-2-TiO_x (400 °C) shifts to lower binding energy while no shift is observed for the samples with 5 and 20 cycles (Figure S15b). Additional annealing of TiO_x-protected Ir is a viable strategy to increase the catalyst's stability. It resulted in decreased dissolution not only for the active sites, but also for the underlying substrate and the protective/activating layer of TiO_x. Although there is partial loss of activity, the stability improvement can lead to longer-term operation for water electrolyzers, and it would be interesting to further apply these capping strategies to other precious metal and non-precious metal electrocatalyst compositions and structures.

3.2.5. Influence of TiO_x ALD decoration on Ir-ATO nano-powders: Activity-stability relationships. After studying the planar model system, we switched to the electrolyzer-relevant nano-powder Ir-ATO system. The nanopowders were dispersed onto FTO electrodes for testing. Like Ir-functionalized FTO, the activity of Ir-decorated ATO nanoparticles improved with the increase of Ir loading (**Figure 6a**). The improvement might arise from more active sites available for catalysis and/or favorable Ir-O-Ir interactions in the denser catalyst network. Increased loading was confirmed by XPS (**Table 1**). Addition of 5 cycles of TiO_x to 1S-ATO resulted in higher OER activity. We note that 3S-ATO-5-TiO_x does not disperse well in the ink for spin-coating which results in inhomogeneous coverage on the electrode and lowered observed activity. Thus, we believe that the SFC data is more representative of the true performance in this case. The XPS analysis of the electrochemically tested 1S-ATO and 3S-ATO shows no significant change in the amount of Ir. No Ir or Ti loss was observed for 1S-ATO-5-TiO_x while according to the CV, its activity is higher than of 1S-ATO. 3S-ATO-5-TiO_x loses a quarter of the initial Ir and half of Ti. The trend in activity/stability for 1S- vs 3S-ATO with TiO_x matches what was measured for 1S-FTO and 3S-FTO. The addition of TiO_x to a thicker layer of IrO_x appears to simultaneously trigger an enhancement of activity and a decrease in stability. This again is consistent with TiO_x able to

form a better capping layer on 1S-FTO and 1S-ATO binding to the support as well as the active sites resulting in improved stability and activity.

We could not reliably study the dissolution profile of 1S-ATO and 1S-ATO-5-TiO_x with the flow cell because they were not sufficiently active, likely due to issues of electrical connectivity using the powders. Thus, we focused on 3S-ATO. Comparing our 3S-ATO catalyst to the previously published IrO_x-ATO catalyst, its activity is lower: IrO_x-ATO reported by Oh *et al*. reaches the mass activity of 39 $A \cdot g_{Ir}$ at η = 280 mV (decreasing to 21 $A \cdot g_{Ir}$ after stability test), while 3S-ATO achieves that mass activity only at η = 350 mV (at pH 1). The loading on 3S-ATO is, however, 50 times lower than on IrO_x-ATO (~ 10 $\mu g \cdot cm^{-2}$ compared to ~ 170 $ng \cdot cm^{-2}_{ATO}$ here).[23]

The addition of 5 ALD cycles of TiO_x to ATO decreased the OER overpotential ~60 mV but also decreased the stability compared to 3S-ATO (**Figure 6c**). The S-number of 3S-ATO after TiO_x decoration was 1.2 times lower than for 3S-FTO. Interestingly, for FTO, TiO_x triggered Sn dissolution, while for ATO Sn dissolution was 13 times lower upon TiO_x addition. However, Sb dissolution increased by 2.5 times in 3S-ATO-5-TiO_x compared to the 3S-ATO sample. These results suggest that TiO_x may bind to FTO and ATO substrates at different sites and influence the substrates' stability during OER. Geiger *et al*. showed that Sb leaches from ATO during OER in acid leading to the formation of a SnO_2-rich surface.[19] The TiO_x capping layer apparently affects the relative stability of ATO and its dissolution pathways.

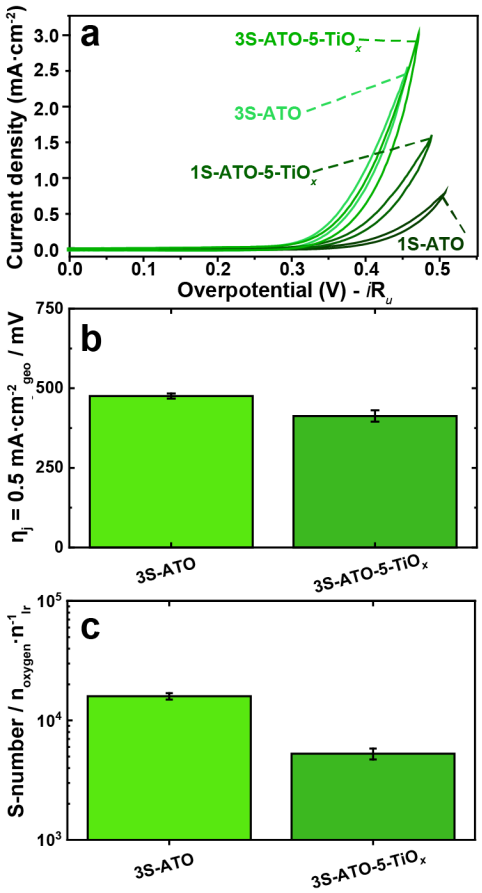

Figure 6. Activity enhancement is accompanied by stability decrease for TiO_x-protected Ir-ATO. a) CV data for Ir-functionalized ATO nano-powder dispersed on FTO electrodes collected in 0.1 M $HClO_4$. b) OER overpotential values at 0.5 $mA \cdot cm^{-2}$ and c) S-numbers calculated for 3S-ATO and 3S-ATO-5-TiO_x.

The binding energy of Ir 4f in 1S-ATO and 3S-ATO samples did not shift to lower values after TiO_x addition (Figure S9) unlike in 1S-FTO and 3S-FTO. The absence of the shift when using a different support might indicate that TiO_x interacts with ATO differently than with FTO influencing IrO_x/support interactions instead of having a direct effect on Ir 4f binding energy by electron donation or withdrawal. As mentioned above, the Ir loss in the TiO_x-protected sample is accompanied by Sb dissolution whereas Sn dissolution is suppressed compared to the 3S-ATO sample. On planar FTO, the increased loss of Ir is accompanied by intensified loss of Sn. On ATO, Ir loss is triggered along with Sb loss. Given that IrO_x is anchored to the support, the leaching of the support would inevitably lead to the structural destabilization of the IrO_x active sites. Even though no binding-energy shift was observed for Ir 4f in the 1S-ATO-5-T TiO_x and 3S-ATO-5-TiO_x compared to the FTO samples, the activity/stability trends are consistent for the two

substrates. The Ir-ATO system with tunable Ir loading protected by TiO_x appears a viable option for reducing the anode catalyst loading in PEMWEs. Its performance can be adjusted through alternating the thicknesses of the catalyst and the protective layer as well as annealing.

4. Conclusions and Outlook

We reported the synthesis of an ultrathin IrO_x catalyst from a molecular precursor on F-doped (planar) or Sb-doped (nanopowder) SnO_2. The synthesis uses only commercial precursors and can be easily controlled and scaled. We investigated the effects of varying the loading of Ir and the addition of TiO_x on the OER activity and stability of Ir-functionalized supports by combining *operando* ICP-MS and post-mortem XPS analyses.

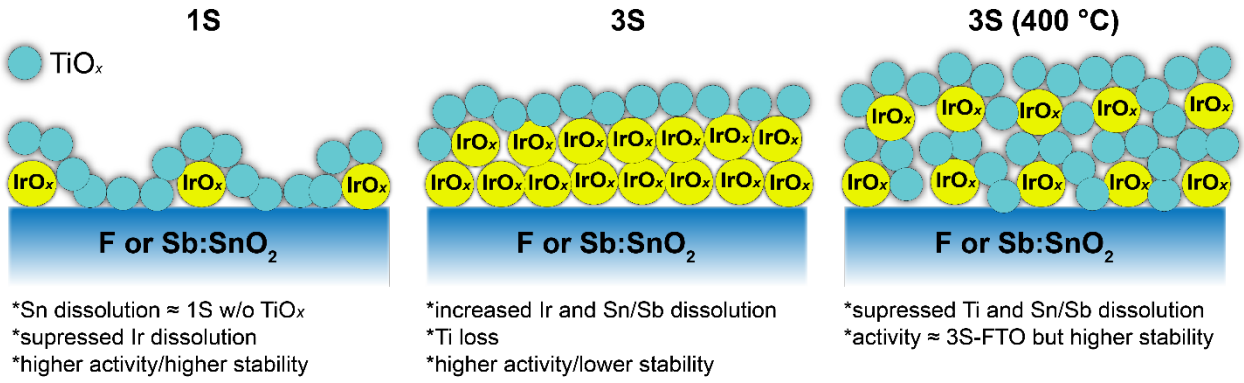

Figure 7. Catalysts' performance is influenced by the binding environment. With small amount of IrO_x on the surface, TiO_x likely binds to the support and IrO_x forming higher stability structure. Once the surface of the support is covered with IrO_x, TiO_x can only bind to IrO_x, which based on our data, is less stable. Upon 400 °C annealing, IrO_x and TiO_x mix to form an acid-resistant catalyst layer.

We have discovered that for both ATO and FTO a thicker IrO_x coverage results not only in activity improvement but also in a higher S-number. We believe that a homogenous network of Ir-O-Ir is responsible for the observed enhancements that effects the active site kinetics. Addition of TiO_x lowers the overpotential to drive OER irrespective of the thickness of the protective layer. However, the resulting stability depends on the thickness of the catalyst layer. After one soak of ATO or FTO in $[(COD)IrCl]_2$, IrO_x likely forms separate islands on the supports allowing the ALD TiO_x capping layer to bind to IrO_x and the underlying metal oxide forming stable protective layer (**Figure 7**) reducing dissolution. Once the surface of the metal oxide is covered with IrO_x, the TiO_x enhances the activity but does not protect the catalyst from dissolution, perhaps because of the IrO_x

layer undergoing dynamic structure changes while driving OER and the lack of direct TiO_x to FTO or ATO linkages. The addition of TiO_x also triggers Sn dissolution in FTO and Sb dissolution in ATO support in addition to enhancing OER activity. We hypothesize that oxygen in the metal oxide substrates might be utilized during the rigorous OER facilitating the loss of Sn and Sb. However, the precise details of how the TiO_x increases the rate of the substrate-support dissolution remains unknown. A thicker TiO_x layer, however, mitigates the dissolution rendering a more stable catalyst. The ability of TiO_x to trigger dissolution has not been previously reported and is an important finding in the context of designing advanced nano-architectured, multicomponent, OER catalysts in acid.

We also discovered that post-ALD annealing yields a more acid-stable matrix that protects Ir from dissolution while keeping active sites accessible for catalysis (**Figure 7**). Thus, we propose and illustrate multiple levers for influencing the interplay between the catalyst's activity and stability.

We, however, realize that the dissolution of the chosen supports, and the fact that some Ir dissolves during OER even for the most stable architectures, makes our catalysts a good model system to study the catalyst/support interactions and further tune the engineered catalyst design, rather than for industrial application directly. The ultra-thin TiO_2-protected catalyst on different conductive metal-oxide supports reported here might also be used for new *in situ* X-ray absorption experiments because all of the Ir is nominally at the "surface" and active for the OER (as opposed to X-ray absorption of minority surface and majority internal sites in typical nanoparticle catalysts convoluting analysis). Others reported that during OER on IrO_x higher oxidation states are reached which leads to high activity but low stability.[59] Determining how TiO_2 affects the oxidation state of Ir during OER (and the oxidation states of the metals in the support) would be useful in designing a high-performing stable catalyst for OER in acid.

ASSOSIATED CONTENT

Supporting Information

The Supporting Information is available free of charge on the ACS Publications website.

Thermogravimetric analysis; additional NMR and UV-vis experiments; summary of XPS with fits for Ir 4f and Ti 2p; TiO_x layer thicknesses; dissolution profiles; and XPS analysis of substrates post electrochemical testing.

AUTHOR INFORMATION

Corresponding Authors

Shannon W. Boettcher – Department of Chemistry and Biochemistry and the Oregon Center for Electrochemistry University of Oregon, Eugene, Oregon 97403, USA;
https://orcid.org/0000-0001-8971-9123;
swb@uoregon.edu

Serhiy Cherevko - Helmholtz-Institute Erlangen-Nürnberg for Renewable Energy (IEK-11), Forschungszentrum Jülich, Erlangen, Germany;
https://orcid.org/0000-0002-7188-4857
s.cherevko@fz-juelich.de

Authors

Raina A. Krivina - Department of Chemistry and Biochemistry and the Oregon Center for Electrochemistry University of Oregon, Eugene, Oregon 97403, USA;
https://orcid.org/0000-0002-4582-3743

Matej Zlatar - Helmholtz-Institute Erlangen-Nürnberg for Renewable Energy (IEK-11), Forschungszentrum Jülich, Erlangen, Germany, and Department of Chemical and Biological Engineering;
https://orcid.org/0000-0003-1041-5149

T. Nathan Stovall - Department of Chemistry and Biochemistry and the Oregon Center for Electrochemistry University of Oregon, Eugene, Oregon 97403, USA;
https://orcid.org/0000-0001-5808-5877

Grace A. Lindquist - Department of Chemistry and Biochemistry and the Oregon Center for Electrochemistry University of Oregon, Eugene, Oregon 97403, USA;
https://orcid.org/0000-0001-5896-2331

Daniel Escalera-Lopez - Department of Interface Science, Fritz-Haber Institute of the Max-Planck Society, 14195 Berlin, Germany;
https://orcid.org/0000-0002-2001-9775

Amanda K. Cook - Department of Chemistry and Biochemistry University of Oregon, Eugene, Oregon 97403, USA;

https://orcid.org/0000-0003-3501-8502

James E. Hutchison - Department of Chemistry and Biochemistry University of Oregon, Eugene, Oregon 97403, USA;

https://orcid.org/0000-0003-2605-3226

ACKNOWLEDGEMENTS

This work was funded by the National Science Foundation grant CHE-1955106 and made use of CAMCOR at the University of Oregon, supported by grants from the W.M. Keck Foundation, the M.J. Murdock Charitable Trust, ONAMI, the Air Force Research Laboratory, and NSF. SC and MZ thank the Deutsche Forschungsgemeinschaft for financial support within the grant CH 1763/4-1. The authors thank Dr. Steve Golledge for assistance with XPS. TEM/EDX imaging was performed by Peter Eschbach at the Oregon State University Electron Microscopy Facility.

Financial Conflict of Interest: The Authors have filed a provisional patent on aspects of the work.

REFERENCES

1. Mayyas, A. T.; Ruth, M. F.; Pivovar, B. S.; Bender, G.; Wipke, K. B. *Manufacturing Cost Analysis for Proton Exchange Membrane Water Electrolyzers*; NREL/TP-6A20-72740 National Renewable Energy Lab, Golden, CO 2019.
2. *Path to Hydrogen Competitiveness: A Cost Perspective*; Hydrogen Council: 2020.
3. Ayers, K.; Danilovic, N.; Ouimet, R.; Carmo, M.; Pivovar, B.; Bornstein, M. Perspectives on Low-Temperature Electrolysis and Potential for Renewable Hydrogen at Scale. *Annu. Rev. Chem. Biomol. Eng.* **2019**, 219-241.
4. Carmo, M.; Fritz, D. L.; Mergel, J.; Stolten, D. A Comprehensive Review on PEM Water Electrolysis. *Int. J. Hydrog. Energy* **2013,** *38* (12), 4901-4934.
5. Reier, T.; Nong, H. N.; Teschner, D.; Schlögl, R.; Strasser, P. Electrocatalytic Oxygen Evolution Reaction in Acidic Environments – Reaction Mechanisms and Catalysts. *Adv. Energy Mater.* **2016,** *7* (1).
6. Rozain, C.; Mayousse, E.; Guillet, N.; Millet, P. Influence of Iridium Oxide Loadings on the Performance of PEM Water Electrolysis Cells: Part I–Pure IrO_2-Based Anodes. *Appl. Catal.* **2016,** *182*, 153-160.
7. Shiva Kumar, S.; Himabindu, V. Hydrogen Production by PEM Water Electrolysis – A Review. *Mater. Sci. Energy Technol.* **2019,** *2* (3), 442-454.
8. Vincent, I.; Bessarabov, D. Low Cost Hydrogen Production by Anion Exchange Membrane Electrolysis: A Review. *Renew. Sust. Energ. Rev.* **2018,** *81*, 1690-1704.
9. Kwasny, M. T.; Tew, G. N. Expanding Metal Cation Options in Polymeric Anion Exchange Membranes. *J. Mater. Chem.* **2017,** *5* (4), 1400-1405.
10. Miller, H. A.; Bouzek, K.; Hnat, J.; Loos, S.; Bernäcker, C. I.; Weißgärber, T.; Röntzsch, L.; Meier-Haack, J. Green Hydrogen from Anion Exchange Membrane Water Electrolysis: A Review of Recent

Developments in Critical Materials and Operating Conditions. *Sustain. Energy Fuels* **2020,** *4* (5), 2114-2133.
11. Du, N.; Roy, C.; Peach, R.; Turnbull, M.; Thiele, S.; Bock, C. Anion-Exchange Membrane Water Electrolyzers. *Chem. Rev.* **2022**.
12. Bernt, M.; Hartig-Weiß, A.; Tovini, M. F.; El-Sayed, H. A.; Schramm, C.; Schröter, J.; Gebauer, C.; Gasteiger, H. A. Current Challenges in Catalyst Development for PEM Water Electrolyzers. *Chem. Ing. Tech.* **2020,** *92* (1-2), 31-39.
13. Ayers, K. The Potential of Proton Exchange Membrane–Based Electrolysis Technology. *Curr. Opin. Electrochem.* **2019,** *18*, 9-15.
14. Pham, C. V.; Escalera-López, D.; Mayrhofer, K.; Cherevko, S.; Thiele, S. Essentials of High Performance Water Electrolyzers – From Catalyst Layer Materials to Electrode Engineering. *Adv. Energy Mater.* **2021,** *11* (44), 2101998.
15. Rodríguez-García, B.; Reyes-Carmona, Á.; Jiménez-Morales, I.; Blasco-Ahicart, M.; Cavaliere, S.; Dupont, M.; Jone, D.; Rozière, J.; Galán-Mascarós, J. R.; Jaouen, F. Cobalt Hexacyanoferrate Supported on Sb-Doped SnO_2 as a Non-Noble Catalyst for Oxygen Evolution in Acidic Medium. *R. Soc. Chem.* **2017**, 589-597.
16. Yang, X., Li, H., Lu, A. -Y., Min, S., Idriss, Z., Hedhili, N. M., Huang, K. -W., Idriss, H., and Li, L. -J. Highly Acid-Durable Carbon Coated Co_3O_4 Nanoarrays as Efficient Oxygen Evolution Electrocatalysts. *Nano Energy* **2016,** *25*, 42-50.
17. Li, A.; Ooka, H.; Bonnet, N.; Hayashi, T.; Sun, Y.; Jiang, Q.; Li, C.; Han, H.; Nakamura, R. Stable Potential Windows for Long-Term Electrocatalysis by Manganese Oxides Under Acidic Conditions. *Angew. Chem. Int. Ed.* **2019,** *58* (15).
18. Blasco-Ahicart, M.; Soriano-López, J.; Carbó, J. J.; Poblet, J. M.; Galan-Mascaros, J. R. Polyoxometalate Electrocatalysts Based on Earth-Abundant Metals for Efficient Water Oxidation in Acidic Media. *Nat. Chem.* **2018,** *10* (1), 24-30.
19. Geiger, S.; Kasian, O.; Mingers, A. M.; Mayrhofer, K. J. J.; Cherevko, S. Stability Limits of Tin-Based Electrocatalyst Supports. *Sci. Rep.* **2017,** *7* (1), 4595.
20. da Silva, G. C.; Venturini, S. I.; Zhang, S.; Löffler, M.; Scheu, C.; Mayrhofer, K. J. J.; Ticianelli, E. A.; Cherevko, S. Oxygen Evolution Reaction on Tin Oxides Supported Iridium Catalysts: Do We Need Dopants? *ChemElectroChem* **2020,** *7* (10), 2330-2339.
21. Ledendecker, M.; Geiger, S.; Hengge, K.; Lim, J.; Cherevko, S.; Mingers, A. M.; Göhl, D.; Fortunato, G. V.; Jalalpoor, D.; Schüth, F.; Scheu, C.; Mayrhofer, K. J. J. Towards Maximized Utilization of Iridium for the Acidic Oxygen Evolution Reaction. *Nano Res.* **2019,** *12* (9), 2275-2280.
22. Hartig-Weiss, A.; Miller, M.; Beyer, H.; Schmitt, A.; Siebel, A.; Freiberg, A. T. S.; Gasteiger, H. A.; El-Sayed, H. A. Iridium Oxide Catalyst Supported on Antimony-Doped Tin Oxide for High Oxygen Evolution Reaction Activity in Acidic Media. *ACS Appl. Nano Mater.* **2020,** *3* (3), 2185-2196.
23. Oh, H.-S.; Nong, H. N.; Reier, T.; Bergmann, A.; Gliech, M.; Ferreira de Araújo, J.; Willinger, E.; Schlögl, R.; Teschner, D.; Strasser, P. Electrochemical Catalyst–Support Effects and Their Stabilizing Role for IrO_x Nanoparticle Catalysts during the Oxygen Evolution Reaction. *J. Am. Chem. Soc.* **2016,** *138* (38), 12552-12563.
24. Abbou, S.; Chattot, R.; Martin, V.; Claudel, F.; Solà-Hernandez, L.; Beauger, C.; Dubau, L.; Maillard, F. Manipulating the Corrosion Resistance of SnO_2 Aerogels through Doping for Efficient and Durable Oxygen Evolution Reaction Electrocatalysis in Acidic Media. *ACS Catal.* **2020,** *10* (13), 7283-7294.
25. Polonský, J.; Mazúr, P.; Paidar, M.; Christensen, E.; Bouzek, K. Performance of a PEM Water Electrolyser Using a TaC-Supported Iridium Oxide Electrocatalyst. *Int. J. Hydrog. Energy* **2014,** *39* (7), 3072-3078.

26. Böhm, D.; Beetz, M.; Gebauer, C.; Bernt, M.; Schröter, J.; Kornherr, M.; Zoller, F.; Bein, T.; Fattakhova-Rohlfing, D. Highly Conductive Titania Supported Iridium Oxide Nanoparticles with Low Overall Iridium Density as OER Catalyst for Large-Scale PEM Electrolysis. *Applied Materials Today* **2021,** *24*, 101134.
27. Oakton, E.; Lebedev, D.; Povia, M.; Abbott, D. F.; Fabbri, E.; Fedorov, A.; Nachtegaal, M.; Copéret, C.; Schmidt, T. J. IrO_2-TiO_2: A High-Surface-Area, Active, and Stable Electrocatalyst for the Oxygen Evolution Reaction. *ACS Catal.* **2017,** *7* (4), 2346-2352.
28. Bernt, M.; Schramm, C.; Schröter, J.; Gebauer, C.; Byrknes, J.; Eickes, C.; Gasteiger, H. A. Effect of the IrO_x Conductivity on the Anode Electrode/Porous Transport Layer Interfacial Resistance in PEM Water Electrolyzers. *J. Electrochem. Soc.* **2021,** *168* (8), 084513.
29. Möckl, M.; Ernst, M. F.; Kornherr, M.; Allebrod, F.; Bernt, M.; Byrknes, J.; Eickes, C.; Gebauer, C.; Moskovtseva, A.; Gasteiger, H. A. Durability Testing of Low-Iridium PEM Water Electrolysis Membrane Electrode Assemblies. *J. Electrochem. Soc.* **2022,** *169* (6), 064505.
30. Finke, C. E.; Omelchenko, S. T.; Jasper, J. T.; Lichterman, M. F.; Read, C. G.; Lewis, N. S.; Hoffmann, M. R. Enhancing the Activity of Oxygen-Evolution and Chlorine-Evolution Electrocatalysts by Atomic Layer Deposition of TiO_2. *Energy Environ. Sci.* **2019,** *12* (1), 358-365.
31. Kasian, O.; Li, T.; Mingers, A. M.; Schweinar, K.; Savan, A.; Ludwig, A.; Mayrhofer, K. Stabilization of an Iridium Oxygen Evolution Catalyst by Titanium Oxides. *J. Phys. Energy* **2021,** *3* (3), 034006.
32. Zhao, Y.; Yang, K. R.; Wang, Z.; Yan, X.; Cao, S.; Ye, Y.; Dong, Q.; Zhang, X.; Thorne, J. E.; Jin, L.; Materna, K. L.; Trimpalis, A.; Bai, H.; Fakra, S. C.; Zhong, X.; Wang, P.; Pan, X.; Guo, J.; Flytzani-Stephanopoulos, M.; Brudvig, G. W.; Batista, V. S.; Wang, D. Stable Iridium Dinuclear Heterogeneous Catalysts Supported on Metal-Oxide Substrate for Solar Water Oxidation. *Proceedings of the National Academy of Sciences* **2018,** *115* (12), 2902-2907.
33. Oener, S. Z.; Foster, M. J.; Boettcher, S. W. Accelerating Water Dissociation in Bipolar Membranes and for Electrocatalysis. *Science* **2020,** *369* (6507), 1099.
34. Ehelebe, K.; Escalera-López, D.; Cherevko, S. Limitations of Aqueous Model Systems in the Stability Assessment of Electrocatalysts for Oxygen Reactions in Fuel Cell and Electrolyzers. *Curr. Opin. Electrochem.* **2021,** *29*, 100832.
35. Lagadec, M. F.; Grimaud, A. Water Electrolysers with Closed and Open Electrochemical Systems. *Nat. Mater.* **2020,** *19* (11), 1140-1150.
36. Mandal, M.; Moore, M.; Secanell, M. Measurement of the Protonic and Electronic Conductivities of PEM Water Electrolyzer Electrodes. *ACS Appl. Mater.* **2020,** *12* (44), 49549-49562.
37. Lindquist, G. A.; Xu, Q.; Oener, S. Z.; Boettcher, S. W. Membrane Electrolyzers for Impure-Water Splitting. *Joule* **2020,** *4* (12), 2549-2561.
38. Fathi Tovini, M.; Hartig-Weiß, A.; Gasteiger, H. A.; El-Sayed, H. A. The Discrepancy in Oxygen Evolution Reaction Catalyst Lifetime Explained: RDE vs MEA - Dynamicity within the Catalyst Layer Matters. *J. Electrochem. Soc.* **2021,** *168* (1), 014512.
39. Ehelebe, K.; Knöppel, J.; Bierling, M.; Mayerhöfer, B.; Böhm, T.; Kulyk, N.; Thiele, S.; Mayrhofer, K. J. J.; Cherevko, S. Platinum Dissolution in Realistic Fuel Cell Catalyst Layers. *Angew. Chem. Int. Ed.* **2021,** *60* (16), 8882-8888.
40. Knöppel, J.; Möckl, M.; Escalera-López, D.; Stojanovski, K.; Bierling, M.; Böhm, T.; Thiele, S.; Rzepka, M.; Cherevko, S. On the Limitations in Assessing Stability of Oxygen Evolution Catalysts Using Aqueous Model Electrochemical Cells. *Nat. Commun.* **2021,** *12* (1), 2231.
41. Sheehan, S. W.; Thomsen, J. M.; Hintermair, U.; Crabtree, R. H.; Brudvig, G. W.; Schmuttenmaer, C. A. A Molecular Catalyst for Water Oxidation That Binds to Metal Oxide Surfaces. *Nat. Commun.* **2015,** *6* (1), 6469.
42. Geiger, S.; Kasian, O.; Ledendecker, M.; Pizzutilo, E.; Mingers, A. M.; Fu, W. T.; Diaz-Morales, O.; Li, Z.; Oellers, T.; Fruchter, L.; Ludwig, A.; Mayrhofer, K. J. J.; Koper, M. T. M.; Cherevko, S. The

Stability Number as a Metric for Electrocatalyst Stability Benchmarking. *Nat. Catal.* **2018,** *1* (7), 508-515.
43. Cherevko, S.; Topalov, A. A.; Zeradjanin, A. R.; Katsounaros, I.; Mayrhofer, K. J. J. Gold Dissolution: Towards Understanding of Noble Metal Corrosion. *RSC Adv.* **2013,** *3* (37), 16516-16527.
44. Klemm, S. O.; Topalov, A. A.; Laska, C. A.; Mayrhofer, K. J. J. Coupling of a High Throughput Microelectrochemical Cell with Online Multielemental Trace Analysis by ICP-MS. *Electrochem. Commun.* **2011,** *13* (12), 1533-1535.
45. Klemm, S. O.; Karschin, A.; Schuppert, A. K.; Topalov, A. A.; Mingers, A. M.; Katsounaros, I.; Mayrhofer, K. J. J. Time and Potential Resolved Dissolution Analysis of Rhodium Using a Microelectrochemical Flow Cell Coupled to an ICP-MS. *J. Electroanal. Chem.* **2012,** *677-680*, 50-55.
46. Saveleva, V. A.; Wang, L.; Kasian, O.; Batuk, M.; Hadermann, J.; Gallet, J. J.; Bournel, F.; Alonso-Vante, N.; Ozouf, G.; Beauger, C.; Mayrhofer, K. J. J.; Cherevko, S.; Gago, A. S.; Friedrich, K. A.; Zafeiratos, S.; Savinova, E. R. Insight into the Mechanisms of High Activity and Stability of Iridium Supported on Antimony-Doped Tin Oxide Aerogel for Anodes of Proton Exchange Membrane Water Electrolyzers. *ACS Catal.* **2020,** *10* (4), 2508-2516.
47. Oh, H.-S.; Nong, H. N.; Strasser, P. Preparation of Mesoporous Sb-, F-, and In-Doped SnO_2 Bulk Powder with High Surface Area for Use as Catalyst Supports in Electrolytic Cells. *Adv. Funct. Mater.* **2015,** *25* (7), 1074-1081.
48. Fernando, N. K.; Cairns, A. B.; Murray, C. A.; Thompson, A. L.; Dickerson, J. L.; Garman, E. F.; Ahmed, N.; Ratcliff, L. E.; Regoutz, A. Structural and Electronic Effects of X-ray Irradiation on Prototypical $[M(COD)Cl]_2$ Catalysts. *J. Phys. Chem.* **2021,** *125* (34), 7473-7488.
49. Rajan, Z. S. H. S.; Binninger, T.; Kooyman, P. J.; Susac, D.; Mohamed, R. Organometallic Chemical Deposition of Crystalline Iridium Oxide Nanoparticles on Antimony-Doped Tin Oxide Support with High-Performance for the Oxygen Evolution Reaction. *Catal. Sci. Technol.* **2020,** *10* (12), 3938-3948.
50. Jeong, S.; Lee, J.-Y.; Lee, S. S.; Choi, Y.; Ryu, B.-H. Impact of Metal Salt Precursor on Low-Temperature Annealed Solution-Derived Ga-doped In_2O_3 Semiconductor for Thin-Film Transistors. *J. Phys. Chem.* **2011,** *115* (23), 11773-11780.
51. Sivula, K.; Zboril, R.; Le Formal, F.; Robert, R.; Weidenkaff, A.; Tucek, J.; Frydrych, J.; Grätzel, M. Photoelectrochemical Water Splitting with Mesoporous Hematite Prepared by a Solution-Based Colloidal Approach. *J. Am. Chem. Soc.* **2010,** *132* (21), 7436-7444.
52. Geiger, S.; Kasian, O.; Shrestha, B. R.; Mingers, A. M.; Mayrhofer, K. J. J.; Cherevko, S. Activity and Stability of Electrochemically and Thermally Treated Iridium for the Oxygen Evolution Reaction. *J. Electrochem. Soc.* **2016,** *163* (11), F3132-F3138.
53. Elmaalouf, M.; Odziomek, M.; Duran, S.; Gayrard, M.; Bahri, M.; Tard, C.; Zitolo, A.; Lassalle-Kaiser, B.; Piquemal, J.-Y.; Ersen, O.; Boissière, C.; Sanchez, C.; Giraud, M.; Faustini, M.; Peron, J. The Origin of the High Electrochemical Activity of Pseudo-Amorphous Iridium Oxides. *Nat. Commun.* **2021,** *12* (1), 3935.
54. George, S. M. Atomic Layer Deposition: An Overview. *Chem. Rev.* **2010,** *110* (1), 111-131.
55. Vuori, H.; Pasanen, A.; Lindblad, M.; Valden, M.; Niemelä, M. V.; Krause, A. O. I. The Effect of Iridium Precursor on Oxide-Supported Iridium Catalysts Prepared by Atomic Layer Deposition. *Appl. Surf. Sci.* **2011,** *257* (9), 4204-4210.
56. Kasian, O.; Geiger, S.; Mayrhofer, K. J. J.; Cherevko, S. Electrochemical On-line ICP-MS in Electrocatalysis Research. *The Chemical Record* **2019,** *19* (10), 2130-2142.
57. Kasian, O.; Grote, J.-P.; Geiger, S.; Cherevko, S.; Mayrhofer, K. J. J. The Common Intermediates of Oxygen Evolution and Dissolution Reactions during Water Electrolysis on Iridium. *Angew. Chem. Int. Ed.* **2018,** *57* (9), 2488-2491.

58. Alia, S. M.; Anderson, G. C. Iridium Oxygen Evolution Activity and Durability Baselines in Rotating Disk Electrode Half-Cells. *J. Electrochem. Soc.* **2019,** *166* (4), F282-F294.
59. Chang, S. H.; Connell, J. G.; Danilovic, N.; Subbaraman, R.; Chang, K.-C.; Stamenkovic, V. R.; Markovic, N. M. Activity–Stability Relationship in the Surface Electrochemistry of the Oxygen Evolution Reaction. *Faraday Discuss.* **2014,** *176* (0), 125-133.
60. Danilovic, N.; Subbaraman, R.; Chang, K. C.; Chang, S. H.; Kang, Y. J.; Snyder, J.; Paulikas, A. P.; Strmcnik, D.; Kim, Y. T.; Myers, D.; Stamenkovic, V. R.; Markovic, N. M. Activity-Stability Trends for the Oxygen Evolution Reaction on Monometallic Oxides in Acidic Environments. *J. Phys. Chem. Lett.* **2014,** *5* (14), 2474–2478.
61. Cherevko, S.; Zeradjanin, A. R.; Topalov, A. A.; Kulyk, N.; Katsounaros, I.; Mayrhofer, K. J. J. Dissolution of Noble Metals during Oxygen Evolution in Acidic Media. *ChemCatChem* **2014,** *6* (8), 2219-2223.
62. Naito, T.; Shinagawa, T.; Nishimoto, T.; Takanabe, K. Recent Advances in Understanding Oxygen Evolution Reaction Mechanisms over Iridium Oxide. *Inorganic Chemistry Frontiers* **2021,** *8* (11), 2900-2917.
63. Kriegel, H.; Kollmann, J.; Raudsepp, R.; Klassen, T.; Schieda, M. Chemical and Photoelectrochemical Instability of Amorphous TiO_2 Layers Quantified by Spectroscopic Ellipsometry. *J. Mater. Chem.* **2020,** *8* (35), 18173-18179.

TOC Figure